

Hamiltonian Monte Carlo enhanced by Exact Diagonalization

Finn L. Temmen,^{1,*} Martina Gisti,^{2,3,†} David J. Luitz,^{2,3,‡} Thomas Luu,^{1,4,§} and Johann Ostmeyer^{3,4,¶}

¹*Institute for Advanced Simulation 4, Forschungszentrum Jülich, 52428 Jülich, Germany*

²*Physikalisches Institut, Universität Bonn 53115 Bonn, Germany*

³*Bethe Center for Theoretical Physics, Universität Bonn 53115 Bonn, Germany*

⁴*Helmholtz-Institut für Strahlen- und Kernphysik, Universität Bonn, 53115 Bonn, Germany*

(Dated: March 19, 2026)

Strongly correlated fermionic systems are of great interest in condensed matter physics and numerical methods are indispensable tools for their study. However, existing approaches such as exact diagonalization (ED) and stochastic quantum Monte Carlo methods each suffer from fundamental limitations: ED is hindered by exponential scaling in system size, while Monte Carlo methods are plagued by sign problems and long autocorrelation times. These limitations restrict the accessible parameter space and developing algorithms that efficiently alleviate them remains a central challenge in computational physics. In this work, we propose a *hybrid* algorithm that combines ED and Hamiltonian Monte Carlo (HMC) to simulate 2D arrays of coupled quantum wires, modeled as interacting fermionic Hubbard chains. We demonstrate how our hybrid implementation of HMC, which we dub H²MC, outperforms either method alone across several key simulation facets. When compared to pure ED, H²MC has a much more favorable computational scaling, which allows us to push simulations to much larger 2D arrays. H²MC also greatly alleviates the sign problem and reduces autocorrelation times when compared to pure HMC formulations utilizing either real or imaginary auxiliary fields. Our formalism demonstrates how complementary strengths of seemingly disparate methods can be leveraged to enable feasible simulations in an extended parameter space.

I. INTRODUCTION

Higher dimensional quantum many-body systems of strongly correlated fermions give rise to a wide range of collective phenomena that remain difficult to access from first principles, as analytical approaches become intractable in regimes where interactions dominate. Consequently, numerical simulations have become an indispensable tool for extracting quantitative insight into such systems, and the development of efficient and reliable algorithms remains a central challenge in computational physics.

Broadly speaking, common numerical approaches can be divided into methods that evaluate many-body quantities directly within the Hilbert space, and stochastic methods that reformulate models in terms of a path integral and evaluate it stochastically using Monte Carlo techniques. Direct methods operate on an explicit representation of the many-body Hilbert space and therefore provide numerically exact results. In particular, exact diagonalization (ED) allows for the computation of observables in the thermodynamic equilibrium up to machine precision. However, the dimension of the Hilbert space grows exponentially with system size, fundamentally limiting the accessible lattice sizes. This scaling barrier, often referred to as the *curse of dimensionality*, restricts direct approaches to comparatively small systems despite their high accuracy.

Tensor network methods (TN) [1] partially alleviate this constraint by exploiting the entanglement structure of quantum states. In some cases (especially in 1D), the ground state of a gapped system can be represented with polynomial rather than exponential effort. Unfortunately, excited state properties like the aforementioned gap are typically much harder to extract from TN simulations [2]. Moreover, while one-dimensional matrix product states (MPS) [3] have been very successful, simulations of 2D systems are significantly more challenging. Projected Entangled Pair State (PEPS) [4–6] are the most natural generalisation of MPS to two dimensions and fermionic versions are readily available [7]. Unlike MPS, however, the exact contraction of 2D PEPS, necessary to compute the expectation values, cannot be performed in polynomial time [8] and all practical algorithms must resort to approximations; periodic boundary conditions are then virtually impossible to implement. Isometric tensor network states and their fermionic counterparts have been proposed precisely to circumvent the contraction difficulties, offering a numerically stable subclass of PEPSs that is canonical by construction in 2D [9, 10] and 3D [11]; however, the isometric constraint imposes fundamental limitations on the states expressivity. Alternative 2D ansätze such as tree tensor networks (TTNs) [12, 13] and their augmented variants (aTTNs) [14], which incorporate a layer of disentanglers to better

* Equal contribution; f.temmen@fz-juelich.de

† Equal contribution; mgisti@uni-bonn.de

‡ david.luitz@uni-bonn.de

§ t.luu@fz-juelich.de

¶ ostmeyer@hiskp.uni-bonn.de

capture the entanglement area law in two dimensions, offer a computationally cheaper alternative to PEPS, albeit these represent a smaller class of quantum states than PEPS. Thus, the simulation of large fermionic 2D systems with a small gap remains very challenging if not infeasible for TNs.

Stochastic approaches overcome the scaling limitation by reformulating the evaluation of thermal traces in terms of path integrals, which are then evaluated via stochastic sampling using Monte Carlo integration [15]. Specifically, auxiliary fields are introduced by means of a Hubbard-Stratonovich transformation to decouple many-body interactions, and subsequently sampled using a Markov chain Monte Carlo algorithm. Among these algorithms, the Hamiltonian Monte Carlo (HMC) method [16] (initially hybrid Monte Carlo) enables efficient global updates through molecular dynamics evolution and has long been established as a standard tool in high energy physics and lattice field theory, while increasingly gaining traction in condensed matter applications [17–25]. Nevertheless, practical simulations face two central challenges. First, complex (or non-positive) statistical weights introduce noise into the estimation of expectation values, giving rise to the notorious sign problem [26, 27], which causes statistical errors to grow. We remark that formally TNs are not free of a sign problem either [28], but its severity is typically negligible in practice. Second, potential barriers and multimodal distributions hinder the efficient exploration of the configuration space, leading to large autocorrelation times and in-practice ergodicity violations that can systematically bias results [29].

A natural strategy to mitigate these difficulties is to hybridize direct and stochastic methods, exploiting the complementary strengths of each method. With this approach, one can access system sizes well beyond the reach of full ED and avoid the sampling pathologies that afflict purely stochastic formulations, rendering a larger portion of the parameter space accessible. In this proof of principle work, we employ ED to develop a hybrid HMC (H²MC) framework for a two-dimensional system of interacting Hubbard chains. The considered model consists of one-dimensional Hubbard chains coupled via density-density interactions, forming a genuinely two-dimensional geometry in which inter-chain correlations are driven purely by interactions. Two dimensional systems are of particular numerical interest, as they are particularly challenging for all known methods but seem to lie in reach for improvements compared to three dimensional systems.

We demonstrate that the hybrid scheme correctly reproduces exact results and yields a significant reduction in both the sign problem and autocorrelation times compared to the fully stochastic treatment, enabling access to regimes that are simultaneously beyond the reach of full ED and problematic for conventional auxiliary field quantum Monte Carlo (AFQMC) approaches. We further incorporate stochastic trace estimators to improve computational scaling of the algorithm, and probe the two-dimensional character of the model on large systems approaching the computational frontier of the method.

Related hybrid schemes combining MPS with AFQMC methods have been explored previously [30], though not in conjunction with the HMC algorithm and its associated advantages. We focus here on the same model as pursued in Ref. [30] for comparability. More broadly, hybridization strategies have recently been pursued for sign problem reduction via MPS trial wavefunctions in AFQMC for fermionic systems [31]. Hybrid quantum-classical approaches utilizing Lanczos and MPS based techniques have similarly been explored for solving electron-phonon systems [32].

The remainder of this paper is organized as follows. In Sec. II we briefly summarize the HMC and ED methods hybridized in this work. In Sec. III we introduce the two-dimensional model of interacting Hubbard chains and derive the H²MC formalism. In Sec. IV we present numerical results, assessing the correctness, sampling efficiency, and computational scaling of the hybrid framework across a range of system sizes. We conclude with a summary and outlook in Sec. V.

II. METHOD

In this section, we review the two central numerical methods employed throughout this work. In particular, we summarize the HMC method [16] used for the stochastic estimation of path integrals and the ED approach for the direct evaluation of thermal traces. For a beginner-friendly introduction to the HMC and its efficient usage we recommend Ref. [33].

A. Hamiltonian Monte Carlo

In the framework of lattice field theory, a model is formulated in terms of a path integral, where expectation values of physical observables are given by

$$\langle \mathcal{O} \rangle_S = Z^{-1} \int \mathcal{D}\phi \mathcal{O}[\phi] e^{-S[\phi]} \quad \text{with} \quad Z = \int \mathcal{D}\phi e^{-S[\phi]}, \quad (1)$$

where ϕ_i , $i = 1, \dots, d$ denote the discretized field variables and $\mathcal{D}\phi = \prod_{i=1}^d d\phi_i$ a high-dimensional integration measure. In most interacting theories, evaluating these integrals analytically is infeasible, and expectation values are

instead estimated numerically using Monte Carlo methods.

The basic idea is to interpret $p[\phi] = e^{-S[\phi]}/Z$ as a probability distribution of field configurations ϕ and to generate an ensemble of representative field configurations $\{\phi^{(n)}\}_{n=1}^{N_{\text{cfg}}}$ following this distribution. This is of course only possible if $p[\phi]$ is non-negative and violations of this condition are common and lead to the so called "sign problem".

Then, expectation values defined in Eq. 1 can be expressed by

$$\langle \mathcal{O} \rangle_S \approx \frac{1}{N_{\text{cfg}}} \sum_{n=1}^{N_{\text{cfg}}} \mathcal{O}[\phi^{(n)}], \quad \text{where } \phi^{(n)} \sim p[\phi]. \quad (2)$$

This requires an algorithm capable of sampling configurations from $p[\phi] = e^{-S[\phi]}/Z$, such as Markov chain Monte Carlo (MCMC) methods. As the name suggests, MCMC methods successively generate a sequence of configurations forming a Markov chain, where each state depends only on the previous one. This is achieved by introducing a stochastic process with transition matrix $\Omega(\phi \rightarrow \phi')$ to move from a configuration ϕ to another one ϕ' . Convergence to a target distribution $p[\phi]$ is guaranteed if the algorithm fulfills two conditions. First, the algorithm has to be ergodic, meaning the algorithm can reach any possible configuration in a finite number of steps. Second, it fulfills the detailed balance condition

$$p[\phi]\Omega(\phi \rightarrow \phi') = p[\phi']\Omega(\phi' \rightarrow \phi). \quad (3)$$

A widely used MCMC algorithm is the HMC method, which introduces a set of conjugate momenta π and considers the extended partition function

$$\mathcal{Z} = Z \int \frac{\mathcal{D}\pi}{\mathcal{N}} e^{-\frac{\pi^2}{2}} = \frac{1}{\mathcal{N}} \int \mathcal{D}\pi \mathcal{D}\phi e^{-H[\phi, \pi]}, \quad (4)$$

where \mathcal{N} is some irrelevant normalization and the Hamiltonian is given by

$$H[\phi, \pi] = \frac{1}{2} \sum_{i=1}^d \pi_i^2 + S[\phi]. \quad (5)$$

Sampling is then performed in the joint (ϕ, π) space by evolving Hamilton's equations of motion

$$\frac{d\pi}{d\tau} = -\frac{\partial H}{\partial \phi} = -\frac{\partial S}{\partial \phi} \quad \text{and} \quad \frac{d\phi}{d\tau} = \frac{\partial H}{\partial \pi} = \pi \quad (6)$$

for a fictitious simulation time τ .

For an exact integration, Hamilton's dynamics conserve the energy of the system, ensuring that the configuration maintains the same weight in \mathcal{Z} (4) and thus reproduces the correct target distribution. In practice, however, the molecular dynamics (MD) equations (6) are integrated numerically by discretizing a trajectory of length t_{MD} into N_{MD} steps with step size $\epsilon = t_{\text{MD}}/N_{\text{MD}}$. This inevitably introduces discretization errors that have to be corrected to maintain detailed balance. Therefore, a newly generated configuration $\tilde{\phi}$ is only accepted according to a Metropolis test with probability

$$p_{\text{HMC}} = \min(1, e^{-\Delta H}), \quad \text{where } \Delta H = H[\tilde{\phi}, \tilde{\pi}] - H[\phi, \pi], \quad (7)$$

and rejected otherwise. If the proposal is accepted, it is appended to the Markov chain, $\phi' = \tilde{\phi}$, otherwise the previous configuration recurs, $\phi' = \phi$. Throughout this work, we employ the standard leapfrog integrator, which is symplectic and reversible. Higher order integrators are readily available [34, 35].

B. Exact diagonalization

Fermionic systems pose significant numerical challenges primarily due to the exponential growth of the many-body Hilbert space with increasing system size. For finite systems, however, the Hamiltonian can be represented exactly in the Fock (occupation-number) basis, allowing fermionic statistics to be treated rigorously. This approach is commonly referred to exact diagonalization and provides numerically exact results up to machine precision.

Within ED, the Hamiltonian describing a fermionic system is constructed explicitly in the many-body Hilbert space using fermionic creation c_i^\dagger and annihilation c_j operators, which obey the canonical anticommutation relations

$$\{c_i, c_j^\dagger\} = \delta_{ij}, \quad \{c_i, c_j\} = \{c_i^\dagger, c_j^\dagger\} = 0, \quad (8)$$

and encode the characteristic minus sign that appears when two fermions are exchanged. The many-body Hilbert space is constructed from the Fock basis, where each basis state corresponds to a definite fermionic occupation configuration. Thermodynamic quantities are obtained from explicit evaluations of thermal traces

$$\langle \mathcal{O} \rangle = Z^{-1} \text{tr} (\mathcal{O} e^{-\beta H}), \quad \text{where} \quad Z = \text{tr} (e^{-\beta H}), \quad (9)$$

and β is the inverse temperature. In practice, the exact matrix representation of the Hamiltonian is constructed by defining operators in the local Hilbert space and iteratively building global operators via tensor products. Fermionic anticommutation relations are preserved by explicitly tracking the fermionic parity, for example through Jordan-Wigner strings or equivalent fermionic sign bookkeeping schemes. While ED provides numerically exact results for small systems, its applicability is fundamentally limited by the exponential growth of the Hilbert space with system size. To circumvent this exponential scaling, TN methods [1] offer an alternative route to estimate thermodynamic quantities by exploiting the entanglement structure of many-body states.

Another strategy to access larger system sizes is to replace the exact evaluation of traces by stochastic trace estimates [36, 37]. In this approach, the trace of an operator \mathcal{O} is approximated by averaging expectation values over an ensemble of random states $|\tilde{\psi}\rangle$,

$$\text{tr}(\mathcal{O}) \approx \frac{1}{N_{\text{states}}} \sum_{k=1}^{N_{\text{states}}} \langle \tilde{\psi}_k | \mathcal{O} | \tilde{\psi}_k \rangle, \quad (10)$$

where the approximation improves systematically as the number of sampled states N_{states} increases.

III. FORMALISM

In the present section, we begin by introducing the model considered throughout this work and derive a suitable formulation amenable to the treatment with AFQMC methods, specifically with HMC.

A. The model

In close analogy to Ref. [30], we consider a system of L_y one-dimensional Hubbard-chains of length L_x , coupled by an inter-chain interaction. The Hamiltonian is given by

$$H = \sum_{j=1}^{L_y} \sum_{i=1}^{L_x} \left[- \sum_{\sigma=\{\uparrow,\downarrow\}} t_{\sigma} \left(c_{ij\sigma}^{\dagger} c_{(i+1)j\sigma} + \text{h.c.} \right) + U n_{ij\uparrow} n_{ij\downarrow} + \mu n_{ij} + V n_{ij} n_{i(j+1)} \right], \quad (11)$$

where $c_{ij\sigma}^{\dagger}$ and $c_{ij\sigma}$ create and annihilate an electron with spin $\sigma \in \{\uparrow, \downarrow\}$ at site i on chain j , respectively. Furthermore, we define the number operators $n_{ij\sigma} = c_{ij\sigma}^{\dagger} c_{ij\sigma}$ and $n_{ij} = \sum_{\sigma} n_{ij\sigma}$. Throughout this work, we impose periodic boundary conditions in both the L_x and the L_y directions. Unless stated otherwise, lattice indices labeling sites along a chain run as $i = 1, \dots, L_x$, while the chain index runs as $j = 1, \dots, L_y$. In addition to the inter-chain interaction, characterized by the interaction strength V , the Hamiltonian contains a nearest neighbor hopping term along the chains with hopping parameters t_{σ} , an on-site interaction of strength U , and a chemical potential μ .

B. Decoupling into 1D chains

Before beginning the derivation, we change to the charge basis by performing the particle-hole transformation

$$a_{ij}^{\dagger} \equiv c_{ij\uparrow}^{\dagger}; \quad a_{ij} \equiv c_{ij\uparrow}; \quad b_{ij}^{\dagger} \equiv c_{ij\downarrow}; \quad b_{ij} \equiv c_{ij\downarrow}^{\dagger}. \quad (12)$$

Here, the ladder operators a_{ij}^{\dagger} (b_{ij}^{\dagger}) and a_{ij} (b_{ij}) create and annihilate a spin- \uparrow electron (spin- \downarrow electron-hole) at site i on chain j , respectively. Furthermore, we define the local charge operators

$$q_{ij} \equiv a_{ij}^{\dagger} a_{ij}, \quad \tilde{q}_{ij} \equiv b_{ij}^{\dagger} b_{ij} \quad \text{and} \quad Q_{ij} \equiv q_{ij} - \tilde{q}_{ij}, \quad (13)$$

and it follows that $n_{ij\uparrow} = q_{ij}$ and $n_{ij\downarrow} = 1 - \tilde{q}_{ij}$. Inserting this into the Hamiltonian (11) then yields

$$H = \sum_{i,j} \left[- \left(t_{\uparrow} a_{ij}^{\dagger} a_{(i+1)j} - t_{\downarrow} b_{ij}^{\dagger} b_{(i+1)j} + \text{h.c.} \right) + (U + \mu + 2V)q_{ij} + (-\mu - 2V)\tilde{q}_{ij} - Uq_{ij}\tilde{q}_{ij} + VQ_{ij}Q_{i(j+1)} \right] + \text{const}, \quad (14)$$

where we can omit the constant as it cancels out in expectation values.

The first step of the derivation is to decouple the one-dimensional chains by rewriting the inter-chain interaction. To this end, we complete the square in the V term,

$$V \sum_{i,j} Q_{ij}Q_{i(j+1)} = V \sum_{i,j} (q_{ij} + \tilde{q}_{ij}) - 2V \sum_{i,j} q_{ij}\tilde{q}_{ij} - \frac{V}{2} \sum_{i,j} (Q_{ij} - Q_{i(j+1)})^2 \quad (15)$$

and split the Hamiltonian into a purely one-dimensional part acting along the chain j ,

$$H_{1\text{D}}^{(j)} = \sum_i \left[- \left(t_{\uparrow} a_{ij}^{\dagger} a_{(i+1)j} - t_{\downarrow} b_{ij}^{\dagger} b_{(i+1)j} + \text{h.c.} \right) + (U + \mu + 3V)q_{ij} + (-\mu - V)\tilde{q}_{ij} - (U + 2V)q_{ij}\tilde{q}_{ij} \right]. \quad (16)$$

and a quadratic term coupling neighboring chains,

$$H_V = -\frac{V}{2} \sum_{i,j} (Q_{ij} - Q_{i(j+1)})^2 \quad (17)$$

such that

$$H = \sum_j H_{1\text{D}}^{(j)} + H_V. \quad (18)$$

The additional terms generated by completing the square have been absorbed into the definition of the one-dimensional Hamiltonian (16).

C. Path integral formulation

Next, we discretize the imaginary time interval $[0, \beta]$ into N_t slices of length $\Delta_t = \beta/N_t$ and apply a second-order Suzuki-Trotter decomposition on each imaginary time slice

$$Z = \text{tr} \left[\prod_{t=1}^{N_t} \left(e^{-\frac{\Delta_t}{2} H_V} e^{-\Delta_t \sum_j H_{1\text{D}}^{(j)}} e^{-\frac{\Delta_t}{2} H_V} + \mathcal{O}(\Delta_t^3) \right) \right]. \quad (19)$$

Using the cyclicity of the trace, the partition function becomes

$$Z = \text{tr} \left[\prod_{t=1}^{N_t} \left(e^{-\Delta_t \sum_j H_{1\text{D}}^{(j)}} e^{-\Delta_t H_V} \right) \right] + \mathcal{O}(\Delta_t^2), \quad (20)$$

where the individual errors in Eq. 19 accumulate to an error $\mathcal{O}(\Delta_t^2)$. Throughout this work, $t = 1, \dots, N_t$ labels the imaginary time slices. In the following, we omit error terms, with the understanding that exact results for the partition function and all observables are recovered only in the limit $N_t \rightarrow \infty$.

The complete square in Eq. 17 allows us to decouple the chains using the Hubbard-Stratonovich (HS) transformation¹

$$\exp \left\{ \Delta_t \frac{V}{2} (Q_{ij} - Q_{i(j+1)})^2 \right\} \propto \int_{-\infty}^{\infty} d\phi_{tij} \exp \left\{ -\frac{1}{2\Delta_t V} \phi_{tij}^2 - \phi_{tij} (Q_{ij} - Q_{i(j+1)}) \right\}, \quad (21)$$

¹ This step constitutes the main difference between the present derivation and that of Ref. [30]. We introduce a set of continuous auxiliary fields ϕ , which enables global updates via the HMC algorithm, in contrast to the local updates employed in discrete auxiliary field simulations of Hubbard-like models.

by introducing an auxiliary field $\phi_{tij} \in \mathbb{R}$ for each lattice site (i, j) and time slice t .

The transformation in Eq. 21 eliminates all terms coupling different chains (i.e. containing products of operators $Q_{ij}Q_{ij'}$), and the Hilbert space factorizes into independent chain contributions. The coupling is generated by the auxiliary fields ϕ_{tij} . We can exploit this tensor product to decompose the trace over the entire Hilbert space from Eq. 20 into a product of traces over the (1D) chain Hilbert spaces:

$$\text{tr} \left[\bigotimes_{j=1}^{L_y} \prod_t \left(e^{-\Delta_t H_{1D}^{(j)}} e^{-\sum_i Q_{ij} \Delta \phi_{tij}} \right) \right] = \prod_{j=1}^{L_y} \text{tr}_j \left[\prod_t \left(e^{-\Delta_t H_{1D}^{(j)}} e^{-\sum_i Q_{ij} \Delta \phi_{tij}} \right) \right], \quad (22)$$

where $\Delta \phi_{tij} \equiv (\phi_{tij} - \phi_{ti(j-1)})$ and tr_j denotes a trace over the reduced Hilbert space of dimension 4^{L_x} associated with the chain j . Combining bosonic and fermionic contributions into the action,

$$S[\phi] \equiv \sum_{t,i,j} \frac{\phi_{tij}^2}{2\Delta_t V} - \sum_j \log \text{tr}_j \left[\prod_t \left(e^{-\Delta_t H_{1D}^{(j)}} e^{-\sum_i Q_{ij} \Delta \phi_{tij}} \right) \right], \quad (23)$$

the partition function Z and expectation values of observables \mathcal{O} are given by the path integral representation from Eq. 1 with the fermionic part of the action evaluated via the thermal trace in Eq. 9.

We have now separated the field theoretic description into independent one-dimensional, fermionic parts, which we will tackle by ED, and bosonic auxiliary fields ϕ_{tij} to be integrated over. This high dimensional integration will be tackled by HMC.

The use of HMC, introduced in Sec. II A, additionally requires computation of the gradient of the action (23) with respect to the auxiliary field variables ϕ_{tij} , which is

$$\partial_{\phi_{tij}} S[\phi] = \frac{1}{\Delta_t V} \phi_{tij} + \langle Q_{ij}(t) \rangle - \langle Q_{i(j+1)}(t) \rangle, \quad (24)$$

where

$$\langle \mathcal{O}_{ij}(t) \rangle \equiv \frac{\text{tr}_j \left[\prod_{t'=1}^t \left(e^{-\Delta_{t'} H_{1D}^{(j)}} e^{-\sum_i Q_{ij} \Delta \phi_{t'ij}} \right) \mathcal{O}_{ij} \prod_{t'=t+1}^{N_t} \left(e^{-\Delta_{t'} H_{1D}^{(j)}} e^{-\sum_i Q_{ij} \Delta \phi_{t'ij}} \right) \right]}{\text{tr}_j \left[\prod_{t'=1}^{N_t} \left(e^{-\Delta_{t'} H_{1D}^{(j)}} e^{-\sum_i Q_{ij} \Delta \phi_{t'ij}} \right) \right]}. \quad (25)$$

Notably, the form of the action and observables is independent of additional terms that could be included in the one-dimensional Hamiltonian (16), such as next-to-nearest-neighbor hopping, nearest-neighbor interaction, or pairing terms, provided they act within the individual chains.

In practice, the explicit evaluation of thermal traces remains limited by the exponential growth of the Hilbert space, as matrix representations rapidly become prohibitively large. To enable efficient computations, we avoid forming dense matrix exponentials and instead expand

$$e^{-\Delta_t H_{1D}^{(j)}} = \mathbb{1} - \Delta_t H_{1D}^{(j)} + \frac{\Delta_t^2}{2} \left(H_{1D}^{(j)} \right)^2 + \mathcal{O}(\Delta_t^3), \quad (26)$$

leading to sparse matrices due to the locality of $H_{1D}^{(j)}$. This drastically reduces memory requirements and computational cost compared to full dense representations. The truncation error of the expansion of order $\mathcal{O}(\Delta_t^3)$ per time slice adds to the Trotter discretization error introduced in Eq. 20, and vanishes in the limit $N_t \rightarrow \infty$.

Before concluding this section, we emphasize that the auxiliary field formulation derived above is not unique. For example, instead of a real HS transformation (21), one may introduce a purely imaginary auxiliary field $i\phi$. Such alternative choices lead to formally equivalent representations of the partition function but can differ substantially in their numerical properties. In preparation for the present work, we explored several decoupling schemes and found the presented formulation to provide the most robust and efficient performance within the parameter regimes considered here. The implications of this ambiguity are discussed in more detail in Sec. IV and Appendix A, where we compare different choices in the context of pure HMC formulations of the model.

In summary, we have derived a hybrid formulation in which the auxiliary fields ϕ are sampled using Monte Carlo methods, while the fermionic sector is computed via a thermal trace of significantly reduced dimensionality.

IV. RESULTS

In this section, we apply the framework introduced above and assess its performance across different system sizes. In Sec. IV A we first validate the formalism and hybrid approach by studying a small system that permits full ED,

enabling a direct benchmark of the computed observables. We then consider a larger system beyond the reach of ED in Sec. IV B and compare physical observables, autocorrelation times, and the severity of the sign problem with those obtained from a pure HMC implementation of the same model. Next, in Sec. IV C we investigate the use of stochastic trace estimators (10) in the computation of gradients and analyze their impact on numerical efficiency and accuracy. Finally, we discuss computational complexity and push the framework toward the computational frontier in Sec. IV D, demonstrating the two-dimensional nature of the model by measuring density-density correlation functions across different chains.

A. Benchmarking against exact diagonalization

We begin by validating the hybrid framework, introduced in Sec. III, on a system of $L_y = 2$ chains with respective lengths $L_x = 2$, for which full ED remains feasible. This enables a direct and unbiased comparison of observables and provides a stringent test of both the formalism and its numerical implementation.

We focus on the representative parameter choices $U = 3$, $V = 1$, $\beta = 4$, and $t = 1$ at and around half-filling, corresponding to $\mu = -2V - U/2$ on a bipartite lattice. These parameters were chosen to probe a correlated yet numerically stable regime. While we refrain from explicitly extrapolating $N_t \rightarrow \infty$ in this benchmark study, we choose two values of $N_t = 32, 40$ to confirm qualitatively that the simulations converge. Throughout this work, simulations use the optimal trajectory length [38]

$$t_{\text{MD}} = \frac{\pi}{2} \sqrt{\frac{\beta V}{N_t}}, \quad (27)$$

and the number of MD steps N_{MD} is tuned to obtain acceptance rates of 60 – 70%. Simulations are initialized from random configurations, thermalized for $N_{\text{therm}} = 10^3$ HMC steps, and subsequently $N_{\text{cfg}} = 10^4$ configurations are recorded.

We first measure the average charge density of spin- \uparrow particles² per site, i.e.

$$\langle q \rangle \equiv \frac{1}{L_x L_y} \sum_{i,j} \langle q_{ij} \rangle, \quad (28)$$

as a function of μ . The results are depicted in Fig. 1. We observe that at and around half-filling, the simulations converge reliably and show excellent agreement with the exact result obtained from ED. For large absolute values of the chemical potential, the $N_t = 32$ simulation exhibits growing deviations from the exact result, reflecting an increasing systematic error due to the Suzuki-Trotter decomposition (20) and the expansion of the exponential (26). In contrast, the $N_t = 40$ simulation maintains very good agreement, illustrating that these deviations can be systematically reduced by increasing N_t .

In addition to the charge density, we also measure the imaginary-time-dependent spatial correlators

$$C(\tau) \equiv \frac{1}{L_x L_y} \sum_{i,j} \langle a_{ij}(\tau) a_{ij}^\dagger(0) \rangle, \quad \text{where} \quad \mathcal{O}(\tau) \equiv e^{\tau H} \mathcal{O} e^{-\tau H}. \quad (29)$$

In Fig. 1 the obtained estimates at half-filling from the hybrid approach are compared to the exact continuum result. Again, we find excellent agreement and observe that both choices of N_t provide accurate results.

Overall, the hybrid method correctly reproduces exact results in the controlled setting of a 2×2 lattice and estimates can be systematically improved by increasing the number of time slices and the number of samples. Having established its validity in the fully controlled setting, we now turn our attention to system sizes beyond the reach of full ED.

B. Comparing with pure HMC

We now compare the performance of the H²MC formalism to two pure HMC formulations of the same model, differing in the choice of HS transformation. Starting from the action in Eq. 23, the on-site interaction of strength U is decoupled using a second HS transformation, introducing an additional auxiliary field χ . As discussed in Sec. III, this decoupling is not unique as the auxiliary field can be chosen to be purely real, purely imaginary or a mixture thereof [39–41]. In this work, we restrict the comparison to the purely real and purely imaginary choices, whose

² The density of spin- \downarrow holes follows from $\langle \bar{q} \rangle = 1 - \langle q \rangle$.

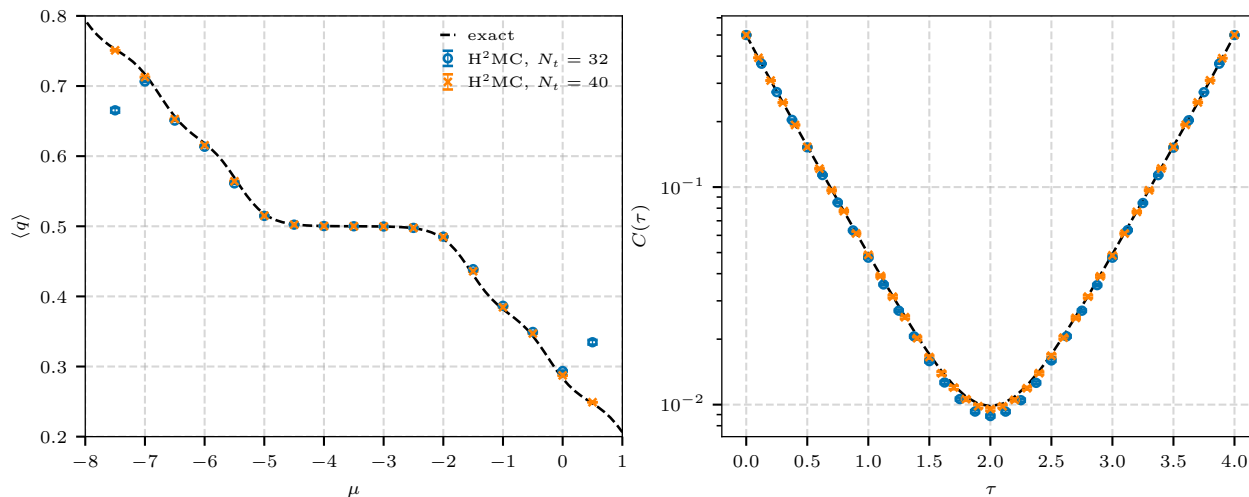


Figure 1. Benchmark of the H²MC framework against full ED on a 2×2 lattice at $U = 3$, $V = 1$, $\beta = 4$, and $t = 1$ around half-filling, corresponding to $\mu = -3.5$. Simulations recorded $N_{\text{cfg}} = 10^4$ configurations for $N_t = 32$ (blue circles) and $N_t = 40$ (orange cross) and are compared to exact continuum results obtained from full ED (black dashed line). Left: Average charge density $\langle q \rangle$ (28) as a function of chemical potential μ . Near half-filling both simulations agree well with the exact result, while deviations grow at large $|\mu|$ for the coarse discretization, reflecting the increasing Suzuki-Trotter error. Right: On-site imaginary-time correlator $C(\tau)$ (29) at half-filling, compared to the exact continuum result. Both values correctly reproduce the correlator accurately across the full imaginary-time extent.

detailed derivations are provided in Appendix A. In the following, we refer to these formulations as *real-field pure HMC* (χ) and *imaginary-field pure HMC* ($i\chi$), respectively.

Generally, auxiliary field formulations of interacting fermionic systems are known to suffer from two central limitations. First, the path-integral weights may become complex (or non-positive), leading to a fermionic sign problem and the degradation of statistical precision. In such cases, the action is split into a real and imaginary part $S = S_R + iS_I$ and configurations are generated according to the real part of the action S_R . Expectation values are then recovered via reweighting

$$\langle \mathcal{O} \rangle_S = \frac{\langle \mathcal{O} e^{-iS_I} \rangle_{S_R}}{\langle e^{-iS_I} \rangle_{S_R}}. \quad (30)$$

Second, multimodal probability distributions lead to increased autocorrelation times in HMC simulations as tunneling times increase with growing separation between modes. Moreover, large autocorrelation times limit the efficient exploration of configuration space and may lead to in-practice ergodicity violations. Utilizing a real or imaginary HS transformation is often a tradeoff between accepting larger autocorrelation times or sign problem. Both effects are generally expected to become more severe with increasing coupling parameter, i.e. for the on-site interaction with increasing U .

To quantify these two effects, we employ complementary statistical diagnostics. The severity of the sign problem is assessed through the average phase

$$\Sigma \equiv |\langle e^{-iS_I} \rangle_{S_R}|. \quad (31)$$

General sampling efficiency and the degree of mode trapping can be characterized by the observable-dependent integrated autocorrelation time $\tau_{\text{int}, \mathcal{O}}$, which quantifies the extent of correlations within a given time series. For an observable \mathcal{O} , with the measurement on the i -th configuration denoted $\mathcal{O}^{(i)}$, it is defined via the autocorrelation function

$$\Gamma_{\mathcal{O}}(t) = \langle [\mathcal{O}^{(i)} - \langle \mathcal{O} \rangle] [\mathcal{O}^{(i+t)} - \langle \mathcal{O} \rangle] \rangle, \quad (32)$$

as

$$\tau_{\text{int}, \mathcal{O}} = \frac{1}{2} \sum_{t=-\infty}^{\infty} \frac{\Gamma_{\mathcal{O}}(t)}{\Gamma_{\mathcal{O}}(0)}. \quad (33)$$

For a detailed introduction we refer the reader to Ref. [42]. Together, these two quantities directly determine the effective number of independent samples, which is proportional to $N_{\text{eff,cf}} \propto \Sigma^2 N_{\text{cf}} / \tau_{\text{int},\mathcal{O}}$, providing a quantitative basis for comparing the sampling efficiency of the hybrid and conventional approach.

We consider a system of $L_y = 6$ chains with length $L_x = 4$, corresponding to 24 lattice sites which is well beyond the reach of full ED. Choosing $\beta = 1$, $U = 3$, $V = 0.2$, and $t = 1$, we tune the chemical potential to half-filling $\mu = -1.9$ and perform both H²MC and pure HMC simulations with $N_t = 32$. For the H²MC formulation, we first thermalize for $N_{\text{therm}} = 10^3$ trajectories before recording $N_{\text{cf}} = 10^4$ configurations. For both pure HMC formulations, we use the same thermalization length and record $N_{\text{cf}} = 10^5$ configurations. All simulations utilize the trajectory length in Eq. 27 and N_{MD} is tuned to obtain acceptance rates of 60 – 70%.

Results for the spatial correlators (29) are depicted in Fig. 2. All three formulations agree within statistical uncertainties in the estimation of the full temporal extent of the spatial correlators. However, the imaginary-field pure HMC exhibits a substantial sign problem, with average phase $\Sigma = 0.0748(37)$, leading to visibly enlarged error bars. In contrast, both the H²MC formulation and the pure HMC with a second real HS transformation did not encounter a sign problem and exhibit comparably small errors. Nevertheless, since the pure HMC formulation generated an order of magnitude more configurations, this indicates increased autocorrelation times due to the additional HS transformation.

To systematically compare sampling properties, we perform a scan in U at half-filling and fixed $V = 0.2$, $\beta = 1$, $t = 1$. For each simulation, we compute the average phase as well as the integrated autocorrelation time of the spatial correlators (29). Since each point of a correlator is associated with its own integrated autocorrelation time, we take the maximal value over all spatial correlators and full time extent

$$\tau_{\text{int},C} \equiv \max_{\tau_{ij}} \tau_{\text{int},C_{ij}}(\tau) \quad (34)$$

to quantify the autocorrelation time of the given simulation.

The results are shown in Fig. 3. We observe that the integrated autocorrelation time remains approximately constant for the H²MC and imaginary-field pure HMC, while it shows an exponential increase in the given parameter region for real-field pure HMC. Conversely, the average phase Σ remains stable for H²MC and real-field pure HMC but deteriorates significantly at large U in the imaginary-field pure HMC formulation. Thus, the two approaches suffer from complementary limitations; either growing autocorrelation times or a worsening sign problem, both leading to reduced statistical precision. In contrast, by avoiding the second HS transformation, the H²MC method circumvents both issues in this parameter regime.

Naturally, the improved sampling properties must be weighed against the increased computational cost of the H²MC algorithm. Specifically, in the performed simulations, the time for generating a single configuration in the H²MC formulation amounted to approximately $t_{\text{H}^2\text{MC}} \approx 3.3\text{s}$, whereas the generation of a single configuration in the pure HMC formulation took $t_{\text{HMC}} \approx 0.03\text{s}$. Taking both generation time and autocorrelation effects into account, we find that - for our implementation - H²MC is superior for $U \gtrsim 3$ at the current system size, while pure HMC remains more efficient in the weak-coupling regime.

We note that the analysis of this section was extended to a broader range of parameters and the results are shown in detail in Appendix B. In the following we will briefly discuss the main findings of this analysis.

First, we performed the same analysis as presented above for larger values of V up to $V = 1$, with qualitatively similar results (see Fig. 6). However, the sign problem in the imaginary-field pure HMC formulation worsens rapidly with increasing V , rendering that formulation impractical, while real-field pure HMC and H²MC continue to agree.

Similarly, for larger inverse temperatures, the sign problem rapidly renders imaginary-field pure HMC simulations infeasible. Moreover, increasing β while keeping Δ_t approximately constant also resulted in increasing autocorrelation times in the real-field pure HMC formulation, while H²MC remained largely unaffected in the considered parameter regime (see Fig. 7). In addition, at large β we encountered numerical instabilities in the naïve inversion of the fermion matrix, which is required in the gradients (see Appendix A). This is a known issue in AFQMC simulations for which stabilization strategies have been developed [43–45]. The H²MC approach circumvents this issue entirely, as the gradient (24) is computed without requiring matrix inversion.

Finally, we emphasize that similar limitations to those observed with increasing U are expected when increasing V in both the H²MC and pure HMC formalism, since they employ a HS transformation to decouple the inter-chain interaction. We verified this expectation by measuring $\tau_{\text{int},C}$ as a function of V (see Fig. 8). We observe that $\tau_{\text{int},C}$ increases drastically around $V \approx 2$, rapidly rendering both H²MC and pure HMC simulations infeasible. However, from a physical standpoint, the inter-chain interaction strength V is naturally expected to be substantially smaller than the on-site interaction U . Consequently, the regime in which the autocorrelation times become problematic for the V decoupling is unlikely to be reached in physically relevant parameter choices and we do not expect this to constitute a significant practical limitation of the framework.

Overall, the H²MC formulation extends the accessible parameter regime by mitigating the sampling limitations inherent to pure HMC approaches. However, despite the improved scaling compared to a full ED calculation, the

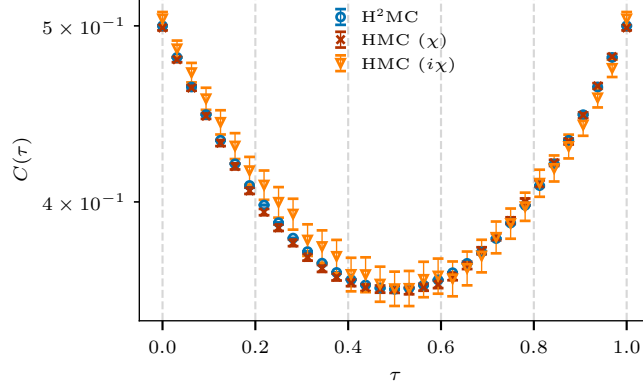


Figure 2. On-site imaginary time correlator $C(\tau)$ (29) at half-filling for a 4×6 lattice at $\beta = 1$, $U = 3$, $V = 0.2$, and $t = 1$, with chemical potential tuned to half-filling $\mu = -1.9$. Simulations compare the H^2MC formulation to the real-field (χ) and imaginary-field ($i\chi$) pure HMC formulations at $N_t = 32$. H^2MC recorded $N_{\text{cfg}} = 10^4$ configurations, while pure HMC generated $N_{\text{cfg}} = 10^5$ configurations each. All three methods agree within statistical uncertainties, while the imaginary field-pure HMC exhibits visibly enlarged error bars due to a substantial sign problem.

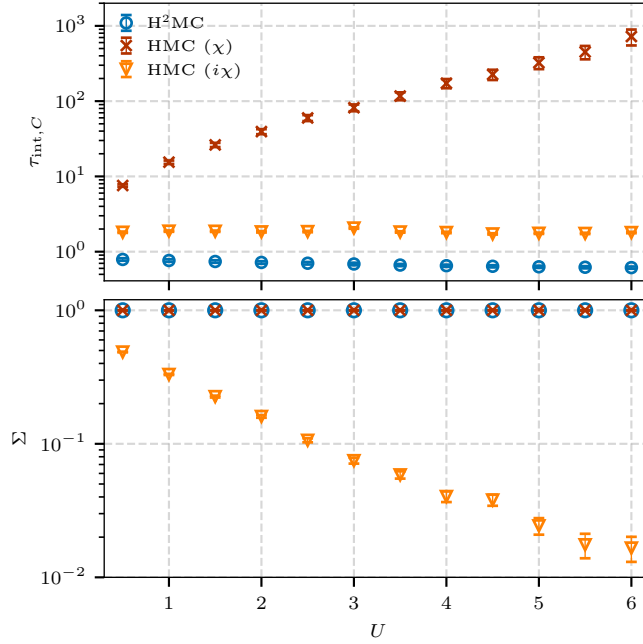


Figure 3. Sampling properties of the H^2MC , real-field pure HMC (χ), and imaginary-field pure HMC ($i\chi$) formulations as a function of the on-site interaction strength U , for a 4×6 lattice at half-filling with $\beta = 1$, $V = 0.2$, and $t = 1$. Top: Maximum integrated autocorrelation time $\tau_{\text{int},C}$ (34) over all spatial correlator and imaginary-time slices. Bottom: Average phase Σ (31) quantifying the sign problem of the respective simulations. The two pure HMC formulations exhibit complementary limitations with increasing U ; We observe growing autocorrelation times for the real-field and deteriorating average phase for the imaginary-field formulation, while H^2MC maintains both a stable short autocorrelation time and an average phase indicating the absence of a sign problem across the full range of U shown.

hybrid algorithm still suffers from the curse of dimensionality in the length of the respective chains. In the next subsection, we will therefore explore stochastic estimates of the thermal traces encountered in the H^2MC formulation to speed up gradient computations.

C. Incorporating stochastic trace estimators

As discussed in Sec. II B, computing the exact action gradient becomes computationally intractable as the chains size grows, due to the exponential scaling of the Hilbert space dimension. To overcome the dimensional bottleneck, we employ stochastic trace estimators (10), which approximate the full trace using a finite ensemble of randomly sampled quantum states. This approach is conceptually analogous to the use of pseudofermion fields in AFQMC simulations, where stochastic estimators are similarly introduced to avoid the explicit computation of fermion determinants. We refer the reader to Refs. [16, 46] for more details.

We evaluate two candidate sampling strategies for constructing these random states: (i) states whose coefficients are drawn from a complex normal distribution (Gaussian), and (ii) states whose coefficients sampled according to a complex Rademacher³ distribution [36, 47–49], i.e. uniformly from $\{1, i, -1, -i\}$. Both distributions satisfy the statistical requirements for an unbiased trace estimator, but may differ in terms of convergence rate, numerical stability, and practical efficiency. For a detailed discussion see for instance the appendix of Ref. [23].

To quantify the accuracy of each approximation scheme, we compute the root-mean-square error (RMSE) of the stochastically estimated trace $\langle Q_{ij}(t) \rangle_{N_{\text{states}}}^{(app)}$ relative to the thermal trace

$$\text{RMSE} = \left(\frac{1}{N_{\text{cfg}}} \sum_{k=1}^{N_{\text{cfg}}} \left(\langle Q_{ij}(t) \rangle_{N_{\text{states}}}^{(app)} - \langle Q_{ij}(t) \rangle_k \right)^2 \right)^{\frac{1}{2}}, \quad (35)$$

where N_{cfg} denotes the number of independent configurations used to evaluate the estimator, and $\langle Q_{ij}(t) \rangle$ is the corresponding exact trace of Eq. (24), serving as reference. This metric provides a direct, configuration-averaged measure of the deviation of the stochastic estimator from the exact result.

In the upper panel of Fig. 4, we report the RMSE as a function of the number of sampled states, N_{states} for three system sizes ($L_x = 4, 5, 6$). Across all system sizes and both sampling distributions, the RMSE decays as $N_{\text{states}}^{-1/2}$, consistent with the standard Monte Carlo convergence rate. This scaling confirms that both estimators are unbiased and that their variance decreases predictably with the number of samples - a particularly important property, as it guarantees that accuracy can be systematically and controllably improved at a well-defined computational cost. Notably, the Rademacher distribution yields a consistently smaller RMSE than the Gaussian distribution for a given N_{states} , suggesting it provides a more efficient basis for trace estimation in this setting.

In the lower panel of Fig. 4, we display the HMC acceptance rate p_{HMC} as a function of N_{states} for both sampling strategies and all system sizes considered. A key observation is that p_{HMC} remains remarkably stable even at very small values of N_{states} , already reaching its large- N_{states} plateau for $N_{\text{states}} \lesssim 10$. This indicates that the stochastic noise introduced by a crude trace approximation does not significantly destabilize the MD evolution, and that the HMC sampler is robust to the variance of the estimator. Furthermore, p_{HMC} varies only mildly with system size, confirming that this robustness is not specific to small systems but persists as the Hilbert space dimension grows. Taken together, these results establish the Rademacher estimator as the preferred choice: it achieves lower statistical error at fixed computational cost while preserving the efficiency of the HMC dynamics.

D. Approaching the computational frontier

We now apply the H²MC framework to larger systems, demonstrating the two-dimensional character of the model. Before presenting the results, however, we first discuss the computational complexity and memory requirements of the algorithm, as these ultimately determine the accessible system sizes.

We begin by considering the gradient computations (24), and in particular the calculation of the thermal expectation values (25) using the stochastic estimators introduced above. The computational cost scales linear in both the number of chains L_y and the number of random states N_{states} , so we focus the analysis on the cost for a single chain j and a $\Omega = 4^{L_x}$ dimensional random state $|\psi\rangle$.

For a given $|\psi\rangle$, each expectation value requires N_t alternating operations: the matrix-vector products $|\psi'\rangle = \exp\{-\sum_i Q_{ij} \Delta\phi_{t'ij}\} |\psi\rangle$, which reduces to elementwise multiplication since Q_{ij} is diagonal, followed by a matrix-vector product $\exp\{-\Delta_t H_{1D}^{(j)}\} |\psi'\rangle$. In practice, the expansion (26) renders the latter matrix exponential sparse. This results in a total of $(c+1)\Omega$ operations per time slice, where c denotes the average number of nonzero elements per row in the expanded form of the exponential. For nearest-neighbor hopping and two fermion species with a second-order expansion of the matrix exponential, one estimates $c \approx 5^2$.

³ The complex Rademacher distribution is also referred to as \mathbb{Z}_4 noise distribution.

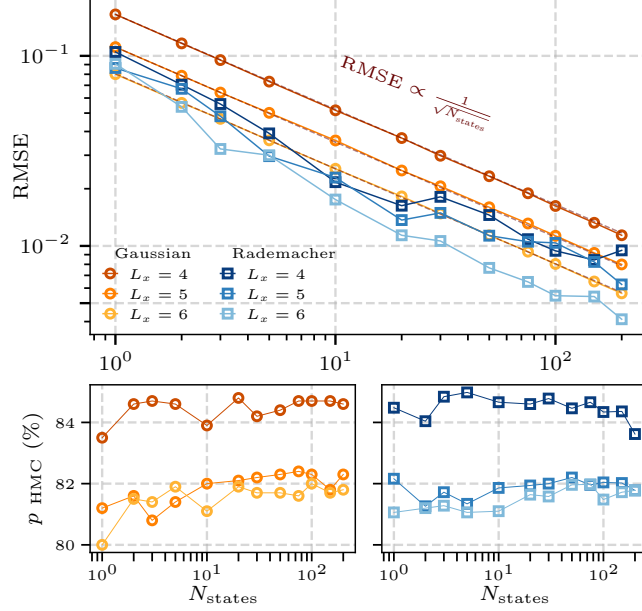


Figure 4. Accuracy and acceptance rate as a function of the number of random states, N_{states} , sampled from a Gaussian (circles) and Rademacher distribution (squares) for one-dimensional subsystems of length L_x . System sizes $L_x = 4, 5, 6$ are indicated by increasingly lighter shades of orange (Gaussian) and blue (Rademacher). Top: Accuracy of the stochastic estimators quantified by the RMSE (35) of the stochastically estimated trace relative to the exact results. The Rademacher distribution achieves a consistently lower RMSE than the Gaussian distribution at fixed N_{states} . Bottom: HMC acceptance rate p_{HMC} as a function of N_{states} for the Gaussian (left) and Rademacher distribution (right). In both cases, p_{HMC} varies only mildly with increasing N_{states} , confirming the robustness of the HMC dynamics to the stochastic noise of the trace estimator.

The total cost can be reduced substantially by pre-computing and storing the prefix and suffix states

$$\begin{aligned}
 \langle \psi_j(t) | &= \langle \psi_j | \prod_{t'=1}^t \left(e^{-\Delta_t H_{1D}^{(j)}} e^{-\sum_i Q_{ij} \Delta \phi_{t'ij}} \right), \\
 | \psi_j(t) \rangle &= \prod_{t'=t+1}^{N_t} \left(e^{-\Delta_t H_{1D}^{(j)}} e^{-\sum_i Q_{ij} \Delta \phi_{t'ij}} \right) | \psi_j \rangle
 \end{aligned} \tag{36}$$

for $t = 1, \dots, N_t$. Once these are available, the expectation value at each imaginary time reduces to a vector dot product, and the full set of N_t expectation values is obtained at an additional cost of $N_t \Omega$ operations. The overall computational complexity is therefore $\mathcal{O}(L_y N_{\text{states}} N_t (2c + 2 + 1) \Omega)$, with memory requirements of $\mathcal{O}(N_t \Omega)$ for storage of the prefix and suffix vectors (36).

The evaluation of the partition function entering the action (23) is more demanding, as it is computed exactly rather than stochastically. It requires N_t sparse matrix-vector products scaling as $c\Omega$, followed by sparse-dense matrix-matrix products scaling as $c\Omega^2$, where repeated multiplications progressively densify the accumulated product. This results in a leading order complexity of $\mathcal{O}(L_y N_t c \Omega^2)$, which dominates over the gradient cost and constitutes the bottleneck of the algorithm. The storage of the accumulated dense matrix further imposes a memory requirement of $\mathcal{O}(\Omega^2)$.

Finally, we note that the computations across chains are embarrassingly parallel, as each chain is treated independently. Parallelization over L_y thus reduces runtimes up to a factor L_y , at the cost of a corresponding increase in total memory consumption.

The above analysis makes clear that the computational frontier of the hybrid algorithm is set by the chain length L_x through the exponential dependence $\Omega = 4^{L_x}$, while the number of chains L_y enters only linearly in either runtime or memory when parallelized. The method is therefore best suited to systems that are extensive in L_y but moderate in L_x . With this in mind, we consider a system of $L_y = 16$ chains of length $L_x = 6$, pushing our current implementation toward the computational frontier. Simulations are performed at $\beta = 1$, $U = 3$, $V = 1$, $t = 1$, and half-filling $\mu = -3.5$, following the same thermalization and sampling procedure outlined in Sec. IV B.

To probe that the method captures the two-dimensional nature of the model, we measure the connected density-density correlation function

$$\langle Q_{ij} Q_{i(j+\Delta_j)} \rangle^c = \langle Q_{ij} Q_{i(j+\Delta_j)} \rangle - \langle Q_{ij} \rangle \langle Q_{i(j+\Delta_j)} \rangle, \tag{37}$$

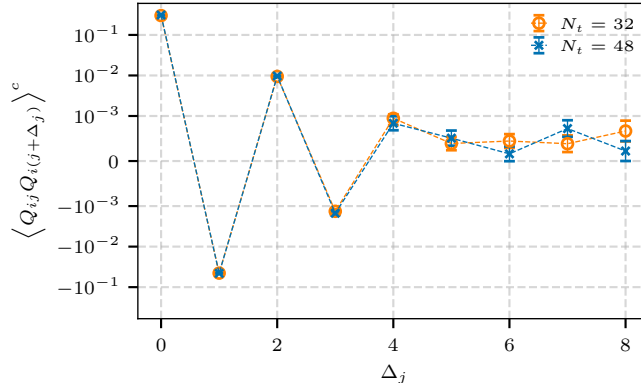


Figure 5. Connected density-density correlation function $\langle Q_{ij}Q_{i'(j+\Delta_j)} \rangle^c$ (37) as a function of chain separation Δ_j for a 6×16 lattice at half-filling with $\beta = 1$, $U = 3$, $V = 1$, and $t = 1$. Results are shown for two values of $N_t = 32, 48$, and have been averaged over equivalent separations imposed by the periodic boundary conditions of the system. The correlator alternates in sign with increasing Δ_j , decaying in magnitude with distance. This reflects the repulsive nature of the V interaction coupling neighboring chains.

between sites on different chains. Since the chains are not connected by any direct hopping and interact exclusively through the inter-chain density-density coupling (17), a nonzero inter-chain connected correlator is an unambiguous signature of interaction-induced correlations. Therefore it provides a direct probe of how the V interaction shapes charge correlations along the L_y dimension.

The connected density-density correlator as a function of chain separation Δ_j is depicted in Fig. 5. The correlator has been averaged over equivalent separations imposed by the periodic boundary conditions of the system, leading to fewer than L_y distinct points. For small chain separations, we observe an oscillating pattern in which the correlator alternates in sign with increasing Δ_j , decaying in magnitude with distance. This behavior is a direct consequence of the repulsive nature of the inter-chain interaction V , where a local presence of charge on one chain favors a depletion on neighboring chains, giving rise to an alternating pattern of correlated charge fluctuations that propagates across the system. Beyond $\Delta_j = 4$, the correlator falls below 10^{-3} and the expected alternating pattern can no longer be resolved, as the inter-chain correlations become negligibly small at large separations.

V. SUMMARY AND OUTLOOK

In this work, we have developed and assessed the H^2MC framework for a spatially two-dimensional system of interacting Hubbard chains. By treating the one-dimensional subsystems exactly via ED and sampling the inter-chain degrees of freedom stochastically using HMC, the framework combines the complementary strengths of both approaches. We benchmarked the method against full ED on small systems, confirming the correctness of the formalism and demonstrating that results can be systematically improved. For larger systems beyond the reach of full ED, we demonstrated that the hybrid formulation significantly reduces both the sign problem and autocorrelation times compared to pure HMC formulations of the same model. We further incorporated stochastic trace estimators into the gradient computations required during the MD evolution, showing that they offer a favorable accuracy-to-cost trade-off. Finally, we discussed the computational complexity of the method and applied it to a large 6×16 system with periodic boundary conditions, where connected density-density correlations between the chains were measured to probe the two-dimensional character of the model.

A similar algorithm has been introduced in Ref. [30], combining MPS with a standard Metropolis-Hastings algorithm based on a discrete HS transformation. There, the discrete nature of the auxiliary fields restricts updates to either local Metropolis steps or heuristic proposal schemes. In contrast, our use of a continuous HS transformation enables utilization of the HMC algorithm, which performs gradient-informed global updates of the auxiliary field with systematically tunable acceptance rates, leading to a more efficient exploration of the configuration space. Furthermore, utilizing ED instead of MPS allows for the use of periodic boundary conditions and avoids the systematic error introduced by finite bond dimension truncation. The primary drawback of this choice is the exponential scaling of ED, which restricts the accessible chain lengths to comparatively small system sizes.

Several directions for addressing this and other limitations naturally suggest themselves for future development. The most immediate bottleneck of the current implementation is the exact computation of the partition function entering the action, which scales as $\mathcal{O}(L_y N_t 4^{2L_x})$ and dominates the overall cost. Extending the stochastic trace

estimation approach to the action is therefore a promising route to alleviate this constraint, potentially pushing accessible chain lengths significantly beyond those demonstrated here.

Furthermore, it has recently been shown that augmenting HMC with global multiplicative updates in the radial direction — so-called *radial updates* — improves the convergence on non-compact manifolds [50, 51] while simultaneously reducing autocorrelation times for some auxiliary field formulations [52]. Since we employ HMC for the stochastic component, incorporating radial updates is a natural extension that we intend to implement in future work.

A more substantial algorithmic improvement would be to replace the ED component entirely with TN methods, as proposed in Ref. [30]. Specifically, employing matrix product operators (MPO) to represent the one-dimensional subsystems and time-evolving block decimation (TEBD) for the imaginary-time evolution would alleviate the exponential scaling of ED. This replacement could dramatically extend the accessible chain lengths while retaining the favorable sampling properties demonstrated in this work. We emphasize, however, that this substitution is not straightforward, since the 1D chains, on which we calculate the thermal quantities exactly, have periodic boundary conditions, which in MPO-based approaches are known to require substantially larger bond dimensions compared to open boundaries.

Finally, extending the model beyond density-density interaction constitutes a natural next step. Of particular interest are the broader class of arrays of coupled quantum wires as systems exhibiting superconductivity and Majorana physics [53–58]. They motivate the development of reliable numerical methods capable of treating strongly correlated quasi-one-dimensional systems. We are confident that our approach to enhance the HMC with ED is generalizable to a vast variety of physical systems as long as they feature relatively weak correlations between small subsystems. Any potentially very strong interactions within the subsystems can be treated with ED and the remaining dynamics are left to the HMC. The H²MC framework developed here represents a step in this direction.

ACKNOWLEDGMENTS

The code used in this work is publicly available at [59]. All data used in the analysis of this study are available from the corresponding author upon reasonable request. We are grateful to Maxime Debertolis, Petar Sinilkov, Lin Wang, and Neill Warrington for valuable discussions. This work was funded by the Deutsche Forschungsgemeinschaft (DFG, German Research Foundation) as part of the CRC 1639 NuMerIQS – Project number 511713970 and under Germany’s Excellence Strategy – Cluster of Excellence Matter and Light for Quantum Computing (ML4Q) EXC 2004/2 – 390534769. We gratefully acknowledge the computing time granted by the JARA Vergabegremium and provided on the JARA Partition part of the supercomputer JURECA at Forschungszentrum Jülich [60].

-
- [1] R. Orús, A practical introduction to tensor networks: Matrix product states and projected entangled pair states, *Annals of Physics* **349**, 117–158 (2014).
 - [2] M. Schneider, J. Ostmeyer, K. Jansen, T. Luu, and C. Urbach, Simulating both parity sectors of the Hubbard Model with Tensor Networks, *Phys. Rev. B* **104**, 155118 (2021).
 - [3] D. Perez-Garcia, F. Verstraete, M. M. Wolf, and J. I. Cirac, Matrix product state representations, *Quant. Inf. Comput.* **7**, 401 (2007), [arXiv:quant-ph/0608197](#).
 - [4] F. Verstraete and J. I. Cirac, Renormalization algorithms for Quantum-Many Body Systems in two and higher dimensions, *arXiv e-prints*, cond-mat/0407066 (2004), [arXiv:cond-mat/0407066 \[cond-mat.str-el\]](#).
 - [5] F. Verstraete and J. I. Cirac, Valence-bond states for quantum computation, *Phys. Rev. A* **70**, 060302 (2004), [arXiv:quant-ph/0311130 \[quant-ph\]](#).
 - [6] P. Corboz, Variational optimization with infinite projected entangled-pair states, *Phys. Rev. B* **94**, 10.1103/PhysRevB.94.035133 (2016).
 - [7] P. Corboz, R. Orús, B. Bauer, and G. Vidal, Simulation of strongly correlated fermions in two spatial dimensions with fermionic projected entangled-pair states, *Phys. Rev. B* **81**, 165104 (2010).
 - [8] N. Schuch, M. M. Wolf, F. Verstraete, and J. I. Cirac, Computational Complexity of Projected Entangled Pair States, *Phys. Rev. Lett.* **98**, 140506 (2007), [arXiv:quant-ph/0611050](#).
 - [9] M. P. Zaletel and F. Pollmann, Isometric tensor network states in two dimensions, *Physical Review Letters* **124**, 10.1103/physrevlett.124.037201 (2020).
 - [10] Z. Dai, Y. Wu, T. Wang, and M. P. Zaletel, Fermionic isometric tensor network states in two dimensions, *Physical Review Letters* **134**, 10.1103/physrevlett.134.026502 (2025).
 - [11] M. S. J. Tepaske and D. J. Luitz, Three-dimensional isometric tensor networks, *Phys. Rev. Res.* **3**, 023236 (2021).
 - [12] L. Tagliacozzo, G. Evenbly, and G. Vidal, Simulation of two-dimensional quantum systems using a tree tensor network that exploits the entropic area law, *Phys. Rev. B* **80**, 235127 (2009), [arXiv:0903.5017](#).
 - [13] V. Murg, F. Verstraete, O. Legeza, and R. M. Noack, Simulating strongly correlated quantum systems with tree tensor networks, *Phys. Rev. B* **82**, 205105 (2010), [arXiv:1006.3095](#).

- [14] N. Reinić, L. Pavešić, D. Jaschke, and S. Montangero, The Augmented Tree Tensor Network Cookbook, [arXiv:2507.21236 \[quant-ph\]](#) (2025), submitted to SciPost Physics Lecture Notes.
- [15] J. Ostmeyer, Stochastic and Tensor Network simulations of the Hubbard Model, in *39th International Symposium on Lattice Field Theory — PoS(LATTICE2022)* (2023) p. 230, [arXiv:2210.06874 \[cond-mat.str-el\]](#).
- [16] S. Duane, A. Kennedy, B. J. Pendleton, and D. Roweth, Hybrid Monte Carlo, *Physics Letters B* **195**, 216 (1987).
- [17] R. C. Brower, C. Rebbi, and D. Schaich, Hybrid Monte Carlo Simulation of Graphene on the Hexagonal Lattice, [arXiv:1101.5131 \[hep-lat\]](#) (2011).
- [18] P. V. Buividovich and M. I. Polikarpov, Monte carlo study of the electron transport properties of monolayer graphene within the tight-binding model, *Phys. Rev. B* **86**, 245117 (2012).
- [19] M. V. Ulybyshev, P. V. Buividovich, M. I. Katsnelson, and M. I. Polikarpov, Monte carlo study of the semimetal-insulator phase transition in monolayer graphene with a realistic interelectron interaction potential, *Phys. Rev. Lett.* **111**, 056801 (2013).
- [20] D. Smith and L. von Smekal, Monte carlo simulation of the tight-binding model of graphene with partially screened coulomb interactions, *Phys. Rev. B* **89**, 195429 (2014).
- [21] P. Buividovich, D. Smith, M. Ulybyshev, and L. von Smekal, Hybrid monte carlo study of competing order in the extended fermionic hubbard model on the hexagonal lattice, *Phys. Rev. B* **98**, 235129 (2018).
- [22] J. Ostmeyer, E. Berkowitz, S. Krieg, T. A. Lähde, T. Luu, and C. Urbach, Semimetal–Mott insulator quantum phase transition of the Hubbard model on the honeycomb lattice, *Phys. Rev. B* **102**, 245105 (2020).
- [23] J. Ostmeyer, E. Berkowitz, S. Krieg, T. A. Lähde, T. Luu, and C. Urbach, Antiferromagnetic character of the quantum phase transition in the Hubbard model on the honeycomb lattice, *Phys. Rev. B* **104**, 155142 (2021).
- [24] M. Rodekamp, E. Berkowitz, C. Gäntgen, S. Krieg, T. Luu, J. Ostmeyer, and G. Pederiva, Single-particle spectrum of doped C₂₀H₁₂-perylene, *Eur. Phys. J. B* **98**, 36 (2025), [arXiv:2406.06711 \[cond-mat.str-el\]](#).
- [25] T.-T. Wang, H. Q. Trung, Q. Xu, M. Long, B. Yang, and Z. Y. Meng, Hybrid monte carlo for fractional quantum hall states, [arXiv:2602.17564 \[cond-mat.str-el\]](#) (2026).
- [26] M. Troyer and U.-J. Wiese, Computational Complexity and Fundamental Limitations to Fermionic Quantum Monte Carlo Simulations, *Phys. Rev. Lett.* **94**, 170201 (2005).
- [27] E. Y. Loh, J. E. Gubernatis, R. T. Scalettar, S. R. White, D. J. Scalapino, and R. L. Sugar, Sign problem in the numerical simulation of many-electron systems, *Phys. Rev. B* **41**, 9301 (1990).
- [28] J. Chen, J. Jiang, D. Hangleiter, and N. Schuch, Sign Problem in Tensor-Network Contraction, *PRX Quantum* **6**, 010312 (2025), [arXiv:2404.19023 \[quant-ph\]](#).
- [29] J.-L. Wynen, E. Berkowitz, C. Koerber, T. A. Laehde, and T. Luu, Avoiding ergodicity problems in lattice discretizations of the Hubbard model, *Physical Review B* **100**, 10.1103/physrevb.100.075141 (2019).
- [30] G. Bollmark, S. Mardazad, J. S. Hofmann, and A. Kantian, Fusing matrix-product states with quantum Monte Carlo: reducing entanglement and sign problem at the same time, [arXiv:2411.00480 \[cond-mat.str-el\]](#) (2024).
- [31] T. Jiang, B. O’Gorman, A. Mahajan, and J. Lee, Unbiasing fermionic auxiliary-field quantum monte carlo with matrix product state trial wavefunctions, *Phys. Rev. Res.* **7**, 013038 (2025).
- [32] H. G. Menzler, S. Mondal, and F. Heidrich-Meisner, Hybrid quantum-classical matrix-product state and Lanczos methods for electron-phonon systems with strong electronic correlations: Application to disordered systems coupled to Einstein phonons, [arXiv:2512.10899 \[cond-mat.str-el\]](#) (2025).
- [33] J. Ostmeyer, The Physicist’s Guide to the HMC, in *41st International Symposium on Lattice Field Theory — PoS(LATTICE2024)* (2025) p. 028, [arXiv:2501.19130 \[hep-lat\]](#).
- [34] I. Omelyan, I. Mryglod, and R. Folk, Symplectic analytically integrable decomposition algorithms: classification, derivation, and application to molecular dynamics, quantum and celestial mechanics simulations, *Computer Physics Communications* **151**, 272 (2003).
- [35] M. Maležič and J. Ostmeyer, Efficient Trotter-Suzuki Schemes for Long-time Quantum Dynamics, [arXiv:2601.18756 \[quant-ph\]](#) (2026).
- [36] S.-J. Dong and K.-F. Liu, Stochastic estimation with Z2 noise, *Physics Letters B* **328**, 130 (1994).
- [37] H. Avron and S. Toledo, Randomized Algorithms for Estimating the Trace of an Implicit Symmetric Positive Semi-Definite Matrix, *J. ACM* **58**, 10.1145/1944345.1944349 (2011).
- [38] J. Ostmeyer and P. Buividovich, Minimal Autocorrelation in Hybrid Monte Carlo simulations using Exact Fourier Acceleration, *Computer Physics Communications* , 109624 (2025), [arXiv:2404.09723 \[hep-lat\]](#).
- [39] S. R. White, R. L. Sugar, and R. T. Scalettar, Algorithm for the simulation of many-electron systems at low temperatures, *Phys. Rev. B* **38**, 11665 (1988).
- [40] S. Beyl, F. Goth, and F. F. Assaad, Revisiting the hybrid quantum monte carlo method for hubbard and electron-phonon models, *Physical Review B* **97**, 10.1103/physrevb.97.085144 (2018).
- [41] P. Buividovich, D. Smith, M. Ulybyshev, and L. von Smekal, Numerical evidence of conformal phase transition in graphene with long-range interactions, *Phys. Rev. B* **99**, 205434 (2019).
- [42] U. Wolff, Monte Carlo errors with less errors, *Computer Physics Communications* **156**, 143 (2004).
- [43] T. Luu, J. Ostmeyer, P. Sinilkov, and F. L. Temmen, Stable Determinant Monte Carlo Simulations at Large Inverse Temperature β (forthcoming).
- [44] C. Bauer, Fast and stable determinant quantum Monte Carlo, *SciPost Phys. Core* **2**, 011 (2020).
- [45] F. F. Assaad and H. G. Evertz, World-line and Determinantal Quantum Monte Carlo Methods for Spins, Phonons and Electrons, in *Computational Many-Particle Physics*, Lecture Notes in Physics, Vol. 739, edited by H. Fehske, R. Schneider, and A. Weiße (Springer, Berlin, Heidelberg, 2008) pp. 277–356.
- [46] A. D. Kennedy, Algorithms for Dynamical Fermions, [arXiv:hep-lat/0607038 \[hep-lat\]](#) (2012).

- [47] M. Hutchinson, A stochastic estimator of the trace of the influence matrix for laplacian smoothing splines, [Communication in Statistics- Simulation and Computation](#) **18**, 1059 (1989).
- [48] T. Iitaka and T. Ebisuzaki, Random phase vector for calculating the trace of a large matrix, [Phys. Rev. E](#) **10.1103/Phys-RevE.69.057701** (2004).
- [49] S.-J. Dong and K.-F. Liu, Stochastic estimation with $z(2)$ noise, [Phys. Lett. B](#) **10.1016/0370-2693(94)90440-5** (1994).
- [50] A. D. Kennedy and X. Yu, On the geometric convergence of HMC on Riemannian manifolds, [PoS LATTICE2024](#), 064 (2025).
- [51] J. Ostmeier, Exponential speed up in Monte Carlo sampling through Radial Updates, [Journal of Physics A: Mathematical and Theoretical](#) **10.1088/1751-8121/add063** (2025), [arXiv:2411.18218 \[physics.comp-ph\]](#).
- [52] F. L. Temmen, E. Berkowitz, A. Kennedy, T. Luu, J. Ostmeier, and X. Yu, Fully ergodic simulations using radial updates, [Phys. Rev. B](#) **112**, 045134 (2025).
- [53] A. Y. Kitaev, Unpaired majorana fermions in quantum wires, [Physics-Uspekhi](#) **44**, 131 (2001).
- [54] A. Keselman, L. Fu, A. Stern, and E. Berg, Inducing time-reversal-invariant topological superconductivity and fermion parity pumping in quantum wires, [Phys. Rev. Lett.](#) **111**, 116402 (2013).
- [55] I. Seroussi, E. Berg, and Y. Oreg, Topological superconducting phases of weakly coupled quantum wires, [Phys. Rev. B](#) **89**, 104523 (2014).
- [56] T. Dvir, G. Wang, N. van Loo, C.-X. Liu, G. P. Mazur, A. Bordin, S. L. Ten Haaf, J.-Y. Wang, D. van Driel, F. Zatelli, *et al.*, Realization of a minimal kitaev chain in coupled quantum dots, [Nature](#) **614**, 445 (2023).
- [57] S. L. Ten Haaf, Q. Wang, A. M. Bozkurt, C.-X. Liu, I. Kulesh, P. Kim, D. Xiao, C. Thomas, M. J. Manfra, T. Dvir, *et al.*, A two-site kitaev chain in a two-dimensional electron gas, [Nature](#) **630**, 329 (2024).
- [58] S. L. Ten Haaf, Y. Zhang, Q. Wang, A. Bordin, C.-X. Liu, I. Kulesh, V. P. Sietses, C. G. Prosko, D. Xiao, C. Thomas, *et al.*, Observation of edge and bulk states in a three-site kitaev chain, [Nature](#) **641**, 890 (2025).
- [59] M. Gisti and F. L. Temmen, [Hybrid Hamiltonian Monte Carlo](#) (2026).
- [60] Jülich Supercomputing Centre, JURECA: Data Centric and Booster Modules implementing the Modular Supercomputing Architecture at Jülich Supercomputing Centre, [Journal of large-scale research facilities](#) **7**, A 182 (2021).
- [61] J. W. Negele and H. Orland, [Quantum Many-particle Systems](#), Frontiers in Physics (CRC Press, 1988).
- [62] J. Zinn-Justin, [Quantum Field Theory and Critical Phenomena](#), International Series of Monographs on Physics (Oxford University Press, 1989).

Appendix A: Derivation of the pure HMC formulations

In this section, we summarize the derivation of a pure HMC formulation of the model introduced in Sec. III. Starting from the one-dimensional Hamiltonian (16), our goal is to decouple the on-site interaction of strength U by means of an additional HS transformation.

In contrast to the HS transformation used for the inter-chain interaction V , we explicitly derive two equivalent pure HMC formulations by utilizing an ambiguity in the preparation for the HS transformation. Specifically, completing the square via

$$-(U + 2V) \sum_i q_{ij} \tilde{q}_{ij} = \pm \frac{1}{2} (U + 2V) \sum_{i,j} (q_{ij} + \tilde{q}_{ij}) \mp \frac{1}{2} (U + 2V) \sum_{i,j} (q_{ij} \pm \tilde{q}_{ij})^2 \quad (\text{A1})$$

results in two different formulations depending on the chosen sign convention

$$H^\pm(j) = H_K^\pm(j) + H_U^\pm(j), \quad (\text{A2})$$

where we defined

$$H_U^+(j) = -\frac{1}{2} (U + 2V) \sum_{i=1}^{L_x} (q_{ij} + \tilde{q}_{ij})^2, \quad H_U^-(j) = \frac{1}{2} (U + 2V) \sum_{i=1}^{L_x} (q_{ij} - \tilde{q}_{ij})^2, \quad (\text{A3})$$

$$H_K^+(j) = \sum_{i=1}^{L_x} \left[- \left(t_\uparrow a_{ij}^\dagger a_{(i+1)j} - t_\downarrow b_{ij}^\dagger b_{(i+1)j} + \text{h.c.} \right) + \left(\frac{3U}{2} + \mu + 4V \right) q_{ij} + \left(\frac{U}{2} - \mu \right) \tilde{q}_{ij} \right], \quad (\text{A4})$$

$$H_K^-(j) = \sum_{i=1}^{L_x} \left[- \left(t_\uparrow a_{ij}^\dagger a_{(i+1)j} - t_\downarrow b_{ij}^\dagger b_{(i+1)j} + \text{h.c.} \right) + \left(\frac{U}{2} + \mu + 2V \right) (q_{ij} - \tilde{q}_{ij}) \right]. \quad (\text{A5})$$

In complete analogy to the treatment of the V interaction, we apply a second-order Suzuki-Trotter decomposition to separate the interaction contribution from the remaining parts of the Hamiltonian. Since the on-site interaction consists solely of density operators, it commutes with the auxiliary field contribution originating from the first HS transformation. Using the cyclicity of the trace, the contributions can therefore be recombined without changing the overall Trotter error, which remains of order $\mathcal{O}(\Delta_t^2)$. For brevity, we omit writing the error explicitly and reiterate that an extrapolation $N_t \rightarrow \infty$ is required to recover the exact result.

The resulting partition function takes the form

$$Z = \int \mathcal{D}\phi \, e^{-S_B[\phi]} \prod_{j=1}^{L_y} \text{tr}_j \left[\prod_{t=1}^{N_t} \left(\exp \{ -\Delta_t H_K^\pm(j) \} \exp \{ -\Delta_t H_U^\pm(j) \} \exp \left\{ \mp \sum_i \Delta \phi_{tij} (q_{ij} - \tilde{q}_{ij}) \right\} \right) \right], \quad (\text{A6})$$

where $S_B[\phi] \equiv \sum_{t,i,j} \frac{\phi_{tij}^2}{2\Delta_t V}$ denotes the bosonic contribution to the action (23). Having isolated the on-site interaction, it can be decoupled via the HS transformation

$$\exp \{ -\Delta_t H_U^\pm(j) \} \propto \int_{-\infty}^{\infty} d\chi_{tij} \exp \left\{ -\frac{\chi_{tij}^2}{2\Delta_t (U + 2V)} - \sigma^\pm \chi_{tij} (q_{ij} \pm \tilde{q}_{ij}) \right\}, \quad (\text{A7})$$

where $\sigma^\pm \equiv \sqrt{\pm 1}$. Therefore, for the $(-)$ convention, we obtain a purely imaginary auxiliary field $i\chi$. As before, the HS transformation comes at the cost of introducing the auxiliary field $\chi_{tij} \in \mathbb{R}$ on every lattice site (i, j) and each imaginary-time slice t that has to be sampled in addition to the ϕ field.

Combining both auxiliary field contributions into a single exponential yields

$$Z = \int \mathcal{D}\phi \mathcal{D}\chi \, e^{-S_B[\phi, \chi]} \prod_{j=1}^{L_y} \text{tr}_j \left[\prod_{t=1}^{N_t} \left(\exp \{ -\Delta_t H_{\text{ID}}^\pm(j) \} \exp \left\{ -\sum_i (\Delta \phi_{tij} (q_{ij} - \tilde{q}_{ij}) + \sigma^\pm \chi_{tij} (q_{ij} \pm \tilde{q}_{ij})) \right\} \right) \right], \quad (\text{A8})$$

where

$$S_B[\phi, \chi] = \sum_{t=1}^{N_t} \sum_{j=1}^{L_y} \sum_{i=1}^{L_x} \left(\frac{\phi_{tij}^2}{2\Delta_t V} + \frac{\chi_{tij}^2}{2\Delta_t (U + 2V)} \right). \quad (\text{A9})$$

For compactness and to facilitate the following derivation, these expressions are rewritten as bilinears in the fermionic creation and annihilation operators

$$Z = \int \mathcal{D}\phi \mathcal{D}\chi e^{-S_B[\phi, \chi]} \prod_{j=1}^{L_y} \text{tr}_j \left[\prod_{t=1}^{N_t} \left(\exp \left\{ a_{xj}^\dagger A_{xy}^{(\pm)} a_{yj} + b_{xj}^\dagger \bar{A}_{xy}^{(\pm)} b_{yj} \right\} \right. \right. \\ \left. \left. \exp \left\{ a_{xj}^\dagger \left(B_{tj}^{(\pm)}[\phi, \chi] \right)_{xy} a_{yj} + b_{xj}^\dagger \left(\bar{B}_{tj}^{(\pm)}[\phi, \chi] \right)_{xy} b_{yj} \right\} \right) \right], \quad (\text{A10})$$

with matrices defined as

$$\begin{aligned} A_{xy}^{(+)} &= \Delta_t t_\uparrow \delta_{\langle x, y \rangle} - \Delta_t \left(\frac{3U}{2} + \mu + 4V \right) \delta_{xy} \\ \bar{A}_{xy}^{(+)} &= -\Delta_t t_\downarrow \delta_{\langle x, y \rangle} - \Delta_t \left(\frac{U}{2} - \mu \right) \delta_{xy} \\ A_{xy}^{(-)} &= \Delta_t t_\uparrow \delta_{\langle x, y \rangle} - \Delta_t \left(\frac{U}{2} + \mu + 2V \right) \delta_{xy} \\ \bar{A}_{xy}^{(-)} &= -\Delta_t t_\downarrow \delta_{\langle x, y \rangle} + \Delta_t \left(\frac{U}{2} + \mu + 2V \right) \delta_{xy} \\ \left(B_{tj}^{(\pm)}[\phi, \chi] \right)_{xy} &= (-\Delta \phi_{txj} - \sigma^\pm \chi_{txj}) \delta_{xy} \\ \left(\bar{B}_{tj}^{(\pm)}[\phi, \chi] \right)_{xy} &= (\Delta \phi_{txj} \mp \sigma^\pm \chi_{txj}) \delta_{xy} \end{aligned} \quad (\text{A11})$$

These matrix definitions will be used throughout the remainder of this section and appear in the final expressions. The derivation can be straightforwardly generalized to include additional terms such as next-to-nearest neighbor hopping.

For each chain j , the thermal trace is evaluated by inserting $2N_t$ sets of fermionic coherent states between successive exponential operators in Eq. A8 using the completeness relation

$$\mathbb{1} = \int \mathcal{D}(\bar{\psi}_{lj} \psi_{lj} \bar{\eta}_{lj} \eta_{lj}) \exp \left\{ - \sum_i (\bar{\psi}_{lj} \psi_{lj} + \bar{\eta}_{lj} \eta_{lj}) \right\} | \psi_{lj}, \eta_{lj} \rangle \langle \psi_{lj}, \eta_{lj} |, \quad (\text{A12})$$

where $\mathcal{D}(\bar{\psi}_{lj} \psi_{lj} \bar{\eta}_{lj} \eta_{lj}) = \prod_{i=1}^{L_x} d\bar{\psi}_{li_j} d\psi_{li_j} d\bar{\eta}_{li_j} d\eta_{li_j}$ and

$$| \psi_{lj}, \eta_{lj} \rangle = \exp \left\{ \sum_i (\psi_{li_j} a_{ij}^\dagger + \eta_{li_j} b_{ij}^\dagger) \right\} | 0 \rangle \quad \text{and} \quad \langle \psi_{lj}, \eta_{lj} | = \langle 0 | \exp \left\{ - \sum_i (a_{ij} \bar{\psi}_{li_j} + b_{ij} \bar{\eta}_{li_j}) \right\}. \quad (\text{A13})$$

Using the definition of the thermal trace $\text{tr}(A) = \sum_n \langle n | A | n \rangle$ together with the identities

$$\langle n | \psi, \eta \rangle \langle \psi, \eta | n \rangle = \langle -\psi, -\eta | n \rangle \langle n | \psi, \eta \rangle \quad \text{and} \quad (\text{A14})$$

$$\langle \psi | \exp \left\{ \sum_{x,y} c_x^\dagger A_{xy} c_y \right\} | \psi \rangle = \exp \left\{ \sum_{x,y} \bar{\psi}_x (e^A)_{xy} \psi_y \right\}, \quad (\text{A15})$$

fermionic ladder operators can be replaced by Grassmann variables, yielding

$$\begin{aligned} Z &= \int \mathcal{D}\phi \mathcal{D}\chi \mathcal{D}(\bar{\psi} \psi \bar{\eta} \eta) e^{-S_B[\phi, \chi]} \exp \left\{ - \sum_{l=1}^{2N_t} \sum_{i,j} (\bar{\psi}_{li_j} \psi_{li_j} + \bar{\eta}_{li_j} \eta_{li_j}) \right\} \\ &\prod_j \exp \left\{ \sum_{t,i} \left(\bar{\psi}_{(2t)xj} \left(e^{A^{(\pm)}} \right)_{xy} \psi_{(2t+1)yj} + \mathcal{B}_t \bar{\psi}_{(2t+1)xj} \left(e^{B_{tj}^{(\pm)}[\phi, \chi]} \right)_{xy} \psi_{(2t+2)yj} \right) \right\} \\ &\prod_j \exp \left\{ \sum_{t,i} \left(+\bar{\eta}_{(2t)xj} \left(e^{\bar{A}^{(\pm)}} \right)_{xy} \eta_{(2t+1)yj} + \mathcal{B}_t \bar{\eta}_{(2t+1)xj} \left(e^{\bar{B}_{tj}^{(\pm)}[\phi, \chi]} \right)_{xy} \eta_{(2t+2)yj} \right) \right\}. \end{aligned} \quad (\text{A16})$$

Here \mathcal{B}_t encodes the anti-periodic boundary conditions in the imaginary-time direction and is defined as $\mathcal{B}_t = +1$, for $t < N_t$ and $\mathcal{B}_{N_t} = -1$. For a detailed introduction to Grassmann variables and fermionic coherent states we refer the reader to Ref. [61].

The Grassmann variables can now be integrated out, producing fermion determinants of dimension $(2N_t L_x)$ for each fermion species and chain j . In practice, it is computationally advantageous to first employ Grassmann δ -functions (see Ref. [62]) to reduce the dimensionality of the fermionic matrices, resulting in

$$Z = \int \mathcal{D}\phi \mathcal{D}\chi e^{-S_B[\phi, \chi] - S_F^{(\pm)}[\phi, \chi]}, \quad (\text{A17})$$

with the fermionic action

$$S_F^{(\pm)}[\phi, \chi] \equiv - \sum_{j=1}^{L_y} \left(\log \det M_j^{(\pm)}[\phi, \chi] + \log \det \bar{M}_j^{(\pm)}[\phi, \chi] \right) \quad (\text{A18})$$

where

$$\begin{aligned} M_j^{(\pm)}[\phi, \chi] &= \mathbb{1} + \prod_{t=1}^{N_t} \left(e^{A^{(\pm)}} e^{B_{tj}^{(\pm)}[\phi, \chi]} \right), \\ \bar{M}_j^{(\pm)}[\phi, \chi] &= \mathbb{1} + \prod_{t=1}^{N_t} \left(e^{\bar{A}^{(\pm)}} e^{\bar{B}_{tj}^{(\pm)}[\phi, \chi]} \right) \end{aligned} \quad (\text{A19})$$

are matrices of dimension L_x . Utilization of HMC requires the computation of force terms, which involve derivatives of the logarithm of the fermion matrix determinant. For a general fermion matrix $M[\phi]$, using Jacobi's formula yields

$$\frac{\partial}{\partial \phi} \log \det M[\phi] = \text{tr} \left[M^{-1}[\phi] \frac{\partial}{\partial \phi} M[\phi] \right], \quad (\text{A20})$$

requiring the explicit computation of the inverse fermion matrix $M^{-1}[\phi]$.

This completes the construction of the real-field (+) and imaginary-field (-) pure HMC formulations employed in Sec. IV B.

Appendix B: Additional results

In this appendix, we collect additional numerical results complementing the comparison between H²MC and the pure HMC formulations of Sec. IV B. Specifically, we extend the analysis performed there to a broader range of parameters, examining the dependence of the integrated autocorrelation $\tau_{\text{int}, C}$ (34) and average phase Σ (31) on the inter-chain interaction strength V , the inverse temperature β , and the on-site interaction U at larger V . Throughout, the system size is kept at a 4×6 lattice.

We first repeat the U scan of Sec. IV B at a larger inter-chain interaction strength $V = 1$, probing whether the qualitative picture observed at smaller V persists in a more strongly coupled regime. The results are shown in Fig. 6. We again observe increasing $\tau_{\text{int}, C}$ for the real-field pure HMC and a diminishing average phase Σ in the imaginary-field pure HMC formulation. In contrast, H²MC retains small autocorrelation time and does not exhibit a sign problem, underlining the results of Sec. IV B. Furthermore, we observe several outlier pure HMC simulations, where numerical instabilities in the inversion of the fermion matrix resulted in near-zero acceptance rates.

Next, we extend the analysis to larger inverse temperatures, performing simulations up to $\beta = 2$ for fixed $U = 3$, $V = 0.2$, and $t = 1$ at half-filling. The Trotter discretization Δ_t is held approximately constant by adjusting N_t to ensure that any observed trends are not contaminated by increasing discretization errors. The results are shown in Fig. 7. The β dependence exhibits a qualitatively similar behavior to the U scan, where pure HMC formulations suffer from complementary limitations, while H²MC does not exhibit a sign problem and maintains small autocorrelation times.

Finally, we consider a scan in the inter-chain interaction strength V at fixed $U = 3$, $\beta = 1$, and $t = 1$. The results for $\tau_{\text{int}, C}$ and Σ as a function of V are shown in Fig. 8. We observe that both H²MC and real-field pure HMC exhibit significantly increasing autocorrelation times with growing V , consistent with the expectation that the HS transformation decoupling the inter-chain interaction introduces similar sampling difficulties as the U decoupling. The autocorrelation times increase drastically around $V \approx 2$, rapidly rendering both formulations infeasible in this regime. In fact, for the H²MC simulation at $V = 3$, we observe an in-practice ergodicity violation that leads to a heavily underestimated autocorrelation time. The imaginary-field pure HMC formulation develops a prohibitively small average phase already at small V and exhibits an outlier simulation at $V = 1.2$, where numerical instabilities resulted in a near-zero acceptance rate.

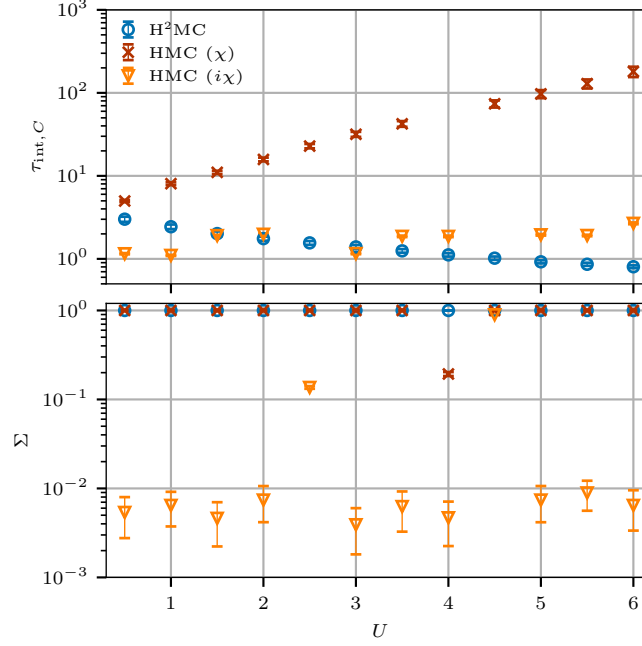


Figure 6. Sampling properties of the H^2MC , real-field pure HMC (χ), and imaginary-field pure HMC ($i\chi$) formulations as a function of the on-site interaction strength U , for a 4×6 lattice at half-filling with $\beta = 1$, $V = 1$, and $t = 1$. Top: Maximum integrated autocorrelation time $\tau_{\text{int},C}$ (34) over all spatial correlator and imaginary-time slices. Bottom: Average phase Σ (31) quantifying the sign problem of the respective simulations. The two pure HMC formulations exhibit complementary limitations with increasing U ; We observe growing autocorrelation times for the real-field and a prohibitively small average phase for the imaginary-field formulation, while H^2MC maintains both a stable short autocorrelation time and an average phase indicating the absence of a sign problem across the full range of U shown.

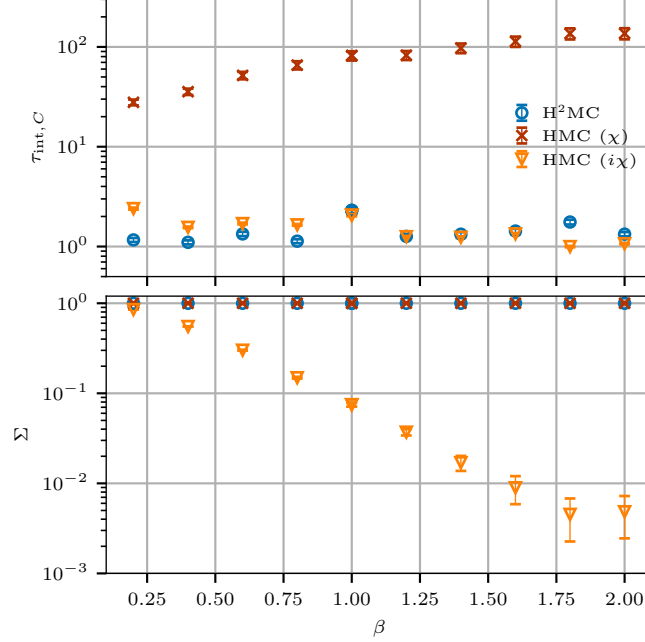


Figure 7. Sampling properties of the H²MC, real-field pure HMC (χ), and imaginary-field pure HMC ($i\chi$) formulations as a function of the inverse temperature β at approximately constant discretization $\Delta_t \approx 1/32$, for a 4×6 lattice at half-filling with $U = 3$, $V = 0.2$, and $t = 1$. Top: Maximum integrated autocorrelation time $\tau_{\text{int},C}$ (34) over all spatial correlator and imaginary-time slices. Bottom: Average phase Σ (31) quantifying the sign problem of the respective simulations. The two pure HMC formulations exhibit complementary limitations with increasing β ; We observe growing autocorrelation times for the real-field and a deteriorating average phase for the imaginary-field formulation, while H²MC maintains both a stable short autocorrelation time and an average phase indicating the absence of a sign problem across the full range of β shown.

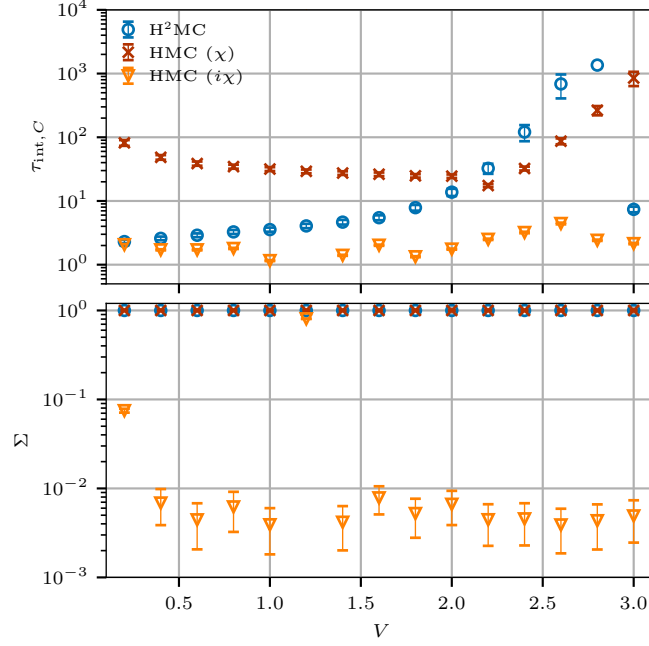


Figure 8. Sampling properties of the H^2MC , real-field pure $\text{HMC}(\chi)$, and imaginary-field pure $\text{HMC}(i\chi)$ formulations as a function of the inter-chain interaction strength V , for a 4×6 lattice at half-filling with $\beta = 1$, $U = 3$, and $t = 1$. Top: Maximum integrated autocorrelation time $\tau_{\text{int},C}$ (34) over all spatial correlator and imaginary-time slices. Bottom: Average phase Σ (31) quantifying the sign problem of the respective simulations. Both H^2MC and real-field pure HMC formulations exhibit significantly increasing autocorrelation times at large V , while the imaginary-field pure HMC develops a prohibitively small average phase already at small V . Real-field pure HMC and H^2MC show an average phase indicating the absence of a sign problem across the entire range of V shown. We also observe an outlier simulation for the imaginary-field pure HMC simulation at $V = 1.2$, where numerical instabilities resulted in a near-zero acceptance rate.